CrossMark

Dependence of tribofilm characteristics on the running-in behavior of aluminum–silicon alloys

Pantcho Stoyanov[1,2,3] · Dominic Linsler[1,2] · Tobias Schlarb[1] · Matthias Scherge[1] · Ruth Schwaiger[2]

Abstract In this study, we evaluate the evolution of the interfacial processes in metallic sliding contacts (i.e., aluminum alloys) in terms of their elemental composition, structural changes, and nanomechanical properties in order to understand the optimal running-in behavior leading to steady-state low friction and high wear resistance. Two different sliding conditions are used, resulting in low and high long-term friction and corresponding well with the low and high wear rates. Ex situ elemental analysis of these sliding experiments was performed by means of X-ray photoelectron spectroscopy. The mechanical properties were evaluated using nanoindentation and microcompression testing. While the elemental analysis revealed an increased oxide content for the near-surface region of the worn surfaces compared to the unworn material, the oxide content was higher for the experiments that resulted in an unfavorable tribological response (i.e., high friction and high wear). Similarly, the sub-surface grain-refined layer under these conditions was thicker compared to the experiment with a short running-in stage and low steady-state friction and wear. These observations correlated well with the nanoindentation and microcompression results, which show higher hardness and yield stress for the high friction

and wear experiment. Correspondingly, low steady-state friction and wear were obtained with the formation of a thin and mechanically stable tribolayer.

Introduction

Aluminum alloys have found a wide range of applications in automotive and aerospace industries due to their low density, thus, light weight, and enhanced corrosion resistance [1, 2]. The addition of silicon improves the wear behavior as well as the casting characteristics making them attractive for complex-shaped sliding components. These sliding contacts typically involve a lubricant to decrease the friction and further increase the endurance of the component.

The sliding of such metallic alloys is known to result in the formation of the so-called third bodies which can be characterized by mechanical mixing, grain refinement, and the formation of chemically induced tribo- and transfer films [3]. Several research efforts have been performed to understand how these third bodies influence the steady-state friction and wear response of aluminum alloys [1, 4–13]. For instance, Rice et al. [14] identified three different zones as a result of sliding and impact wear: base material, the deformed intermediate region, also described as "tribologically transformed structures (TTS)" [15], and the tribolayer consisting of high oxide content as well as transfer material. In addition, the authors reported void formation at the interface of the tribolayer and the deformed intermediate region. Similarly, Venkataraman et al. [9] studied the various deformation zones beneath the worn surface and correlated them to the wear behavior of Al–SiC particulate composites. The authors observed a mechanically mixed layer (MML) on the worn surface, which

✉ Pantcho Stoyanov
pantcho.stoyanov@kennametal.com

[1] Fraunhofer-Institute for Mechanics of Materials IWM - MicroTribology Center μTC, Wöhlerstrasse 11, 79108 Freiburg, Germany

[2] Institute for Applied Materials IAM, Karlsruhe Institute of Technology KIT, Kaiserstrasse 12, 76131 Karlsruhe, Germany

[3] Present Address: Kennametal Inc., 1600 Technology Way, Latrobe, PA 15650, USA

was approximately six times harder than the bulk material. Interestingly, this layer was absent when testing aluminum. In this case, the surface layer was identified as a shear layer composed of two sub-layers, a soft and a hardened one. Such a shear layer was also present beneath the MML layer of the Al–SiC specimen. More recently, Shockley et al. [4] studied the dynamic events at the sliding interface of cold-sprayed Al–Al$_2$O$_3$ composite coatings by means of an in situ tribometer. Using a transparent counterface, the authors were able to identify correlations between the formation of transfer films and fluctuations in the tribological response of the system. The presence of Al$_2$O$_3$ particles promoted the formation of a stable transfer film and uniform third body, as well as lower wear rates and stable friction.

Current understanding of the third bodies is mainly based on analysis during steady-state sliding of a system. As indicated by Blau [16], many of the interfacial processes during the running-in result in friction fluctuations and govern the duration of this period until a steady state is reached. These changes in the interfacial process throughout the running-in can certainly influence the third body characteristics during steady state and, thus, influence the long-term friction and wear response of the system. In some instances, the running-in period is extremely long or steady state is not achieved at all. The interfacial processes in the running-in period are influenced by many variables such as the materials involved, contact pressures, sliding velocities, and environmental conditions [16, 17]. Yet, there are no conclusive correlations between the tribosystem characteristics and the duration of the running-in period as well as the consequential low steady-state friction and wear response.

The aim of this study is to investigate the influence of altered interfacial processes (e.g., mechanical mixing and chemical modification) induced during running-in on the long-term friction and wear response. We examined the interfacial phenomena in terms of the chemical changes and structural characteristics for tribosystems with sliding conditions resulting in short running-in period as well as sliding conditions not reaching a steady state. In addition, nanoindentation and microcompression tests were performed on the worn and unworn surfaces in order to provide a better understanding of the third body behavior. The indentation and compression response of the systems correlated well with the chemical and structural changes of the sub-surface regions.

Experimental procedure

The sliding experiments in this study were performed using a pin-on-disk tribometer designed by TETRA (TETRA GmbH, Ilmenau, Germany). The tests were performed in normal ambient environments (i.e., relative humidity and temperature of $\sim$50 % and $\sim$25 °C, respectively) and lubricated sliding conditions with Castrol Edge FST 5W30 motor oil (70 °C) as a lubricant. A 100Cr6 flat counterface was used in the sliding experiments, and the surface was polished using a "belt finishing process," yielding average roughness R_a and R_{RMS} of 16 and 40 nm, respectively. The chemical composition of the belt finished surface is 5 at.% Cr and 15 at.% C with the balance being Fe. The diameter of the flat surface was 4.9 mm, and the hardness was measured to be between 6 and 8 GPa at indentation depth values below 300 nm. Two different contact pressures were applied (i.e., 15 and 35 MPa) by varying the normal load. The sliding speed was kept constant at 0.4 m s^{-1} and the duration of each test was approximately 12 h. The sliding experiments were performed on the as-cast AlSi$_9$Cu$_3$ alloys, which were machined down to a surface roughness of $R_a = 20$ nm corresponding to $R_{RMS} = 25$ nm utilizing monocrystalline diamond tools (Ultra-precision machining, Fraunhofer IPT). It should be noted that this sample preparation process can lead to the formation of residual stresses and some grain refinement near the surface.

The hardness and yield strength of the third bodies induced by the wear tests were examined using nanoindentation and microcompression testing. A G200 Nanoindenter XP (Agilent Technologies, Santa Clara, CA, USA) was used and operated in the continuous stiffness measurement (CSM) mode. The samples were indented with a diamond Berkovich tip (tip radius $\sim$150 nm) at a constant indentation strain rate of 0.025 s^{-1} to a depth of 2000 nm. For every condition, 20 indents were performed. For the microcompression experiments, a diamond flat punch tip of 10 μm diameter was used.

The free-standing microcompression pillars were machined using a focused ion beam (FIB) platform (Helios Nanolab 650 Dual Beam, FEI, Hillsboro, OR). Prior to FIB-machining, the areas of interest were covered with a thin protective Pt layer using electron-beam-assisted deposition. The pillars were machined in a two-step process starting with a ring of 35 and 15 μm outer and inner diameters, respectively, using an acceleration voltage of 30 kV and beam current of 5 nA. In the second step, the pillars of 1 μm diameter were machined into the resulting pedestal at lower beam currents down to 80 pA to minimize Ga$^+$-ion damage. Adjusting the dwell times, an aspect ratio (height:diameter) of 2.5:1 was achieved. The pillars had the shape of a truncated cone with a taper angle of $\sim$3°, which is typical of the preparation method. The actual dimensions of each pillar were measured prior to testing in the scanning electron microscope (SEM). For this study, we tested a total of 15 pillars (i.e., five for each condition). The pillars were compressed to a preset maximum indenter displacement at a displacement rate of 10 nm s^{-1}.

Ex situ chemical analysis of the worn surfaces was performed using X-ray photoelectron spectroscopy (XPS) (PHI 5000 Versaprobe System with 15 keV monochromatic Al-Kα-X-ray excitation and an energy resolution of 0.2 eV); depth profiles were obtained by iterative removal of surface layers by ion etching (2 keV Ar$^+$) and continuous XPS analysis on an area of 200×200 μm^2. The XPS results of the worn surfaces were compared to the composition of the unworn surface analyzed using the same methodology. The wear depth was determined from images obtained with a white-light interferometer (WLI) (Sensofar PLµ 2300). The microstructures of the deformed and undeformed materials were investigated using FIB and SEM.

Results

Figure 1(a) shows the friction force versus time for the sliding experiments performed with contact pressures of 15 and 35 MPa. Initially, the friction force of 50 N for 35 MPa contact pressure is twice as high as that for the 15 MPa sliding condition. The corresponding coefficient of friction can be seen in the inset. Upon further sliding, the friction force at a contact pressure of 35 MPa shows a drastic decrease for the first two hours to a value of approximately 3 N. Subsequently, while the friction coefficient under these contact conditions slightly increases, it remains below 0.01 for the remainder of the experiment, indicating steady-state sliding. The sliding test with a 15 MPa contact pressure, on the other hand, shows a slightly different behavior; while it gradually decreases upon initial sliding, it fluctuates up and down over the full test period of 7 h. After these long experiments, the samples were subjected to a 5-load-speed-combinations test (resembling Stribeck curves [18], not shown here) in order to measure friction forces under comparable conditions. The results of the friction versus load corresponded well with the behavior in Fig. 1a, namely higher friction forces with larger fluctuations for the worn surface, created initially with 15 MPa contact pressure, exhibiting higher friction values for all parameters in the load-speed-combinations test. Figure 1b shows the WLI results of the wear tracks, represented as the cross sections for the two sliding conditions. The profiles clearly indicate more wear and higher roughness values for a 15 MPa contact pressure compared to the one with 35 MPa, which correlates well with the higher friction forces.

Further ex situ analysis of the worn surfaces is performed by means of XPS depth profiles and cross-sectional imaging of the near-surface region. The XPS depth profiles of the unworn surface and the wear tracks are shown in Fig. 2. The worn surfaces clearly show thicker oxide layers
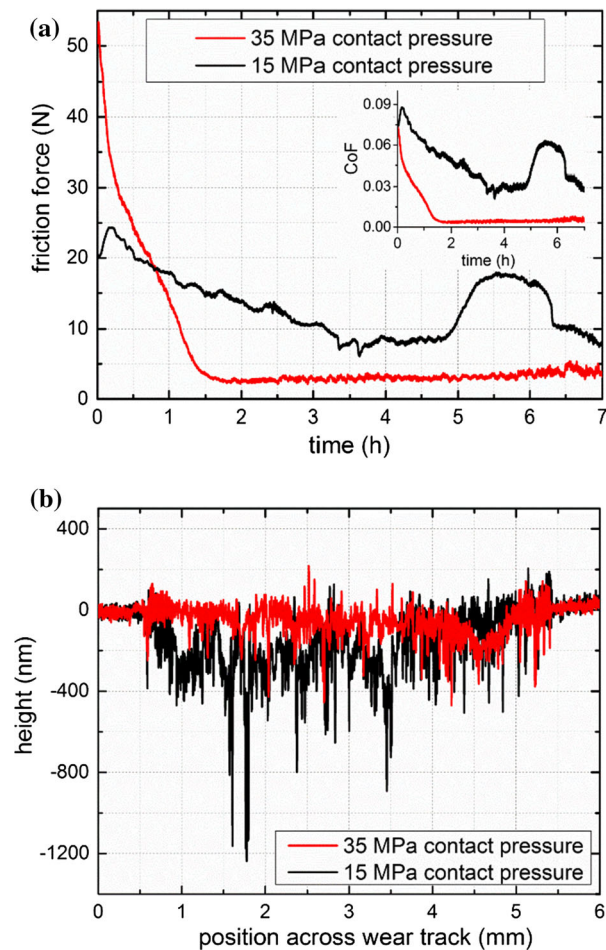
Fig. 1 a Friction force and coefficient of friction versus time and **b** ex situ cross-sectional profiles of the wear tracks obtained by means of WLI

in the near-surface region compared to the unworn surface; while the oxide concentration of the unworn surface drops below 10 at.% at ~ 10 nm, the oxide of the worn surfaces remains above 10 at.% at 300 nm for both sliding conditions. Similarly, the concentration of oxidized aluminum remains present at larger depths compared to the unworn surface. The presence of calcium (i.e., originating from the oil) and oxidized aluminum at comparable depths indicates the formation of a tribofilm consisting of mixed oxides of calcium and aluminum. The silicon concentration near the surface is proportional to the metallically bonded aluminum and is lower in the near-surface region within the wear tracks compared to the unworn state. Chemical analysis of the counterface by means of XPS was also performed (not presented here), which yielded no significant amount of aluminum indicating no evidence of an aluminum transfer film. Interestingly, the oxide content of the worn counterface was higher compared to the unworn surface probably due to the presence of phosphates (i.e., originating from the lubricant). Cross-sectional SEM
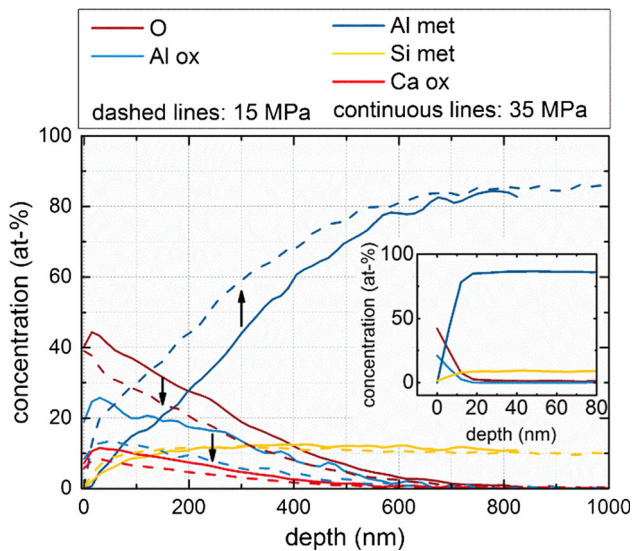
Fig. 2 Comparison of the depth profiles of metallic and oxidized Al, O, Ca, and Si measured by XPS on the worn surface created with a 15 MPa and 35 MPa contact pressure. The *inset* shows the depth profile of an unworn disk

images are shown in Fig. 3 for both the worn and unworn Al surfaces. The micrographs show a typical structure of $AlSi_9Cu_3$ alloys consisting of (alpha) aluminum matrix with needle-like eutectic silicon particles. The micrograph of the unworn surface (Fig. 3a) shows slight microstructural changes in the near-surface region, which have very likely been caused by the sample cutting process. The worn surfaces on the other hand reveal grain refinement in the Al matrix caused by the sliding (Fig. 3b–d). The cross-sectional image of the experiment conducted at 35 MPa contact pressure (Fig. 3b) shows a ∼1-μm-thick fine-grained layer with a clear transition to the underlying material. The fine-grained layer for the experiments performed at 15 MPa contact pressure (Fig. 3c) is significantly thicker and inhomogeneous varying in thickness between ∼1.2 and ∼2.5 μm without a sharp transition to the underlying material. Also in regions of the sample that exhibit pronounced microstructural inhomogeneities (Fig. 3d), the grain refinement is clearly visible as exemplified for the case of 15 MPa contact pressure.

Young's modulus and hardness from the nanoindentation tests are shown in Fig. 4a, b as a function of the indentation depth for the worn and unworn surfaces. The data of 20 indents per test condition averaged in 50-nm windows are shown with error bars representing one standard deviation. The values of Young's modulus agree well for both sliding conditions for depths greater than approximately 500 nm, while Young's modulus of the unworn sample is lower. Similarly, the hardness of the unworn sample is lower after approximately the same depth of indentation. The hardness is clearly different for

the three samples with the 15 MPa sliding condition being the highest. However, the scatter of the results is significant. The scatter for the values of the 15 MPa sample is higher compared to that of the 35 MPa sample up to an indentation depth of 500 nm. Similarly, the scatter in the values of the 35 MPa test is higher compared to the unworn surface up to the same indentation depth. At higher depths, the standard deviation in the values is similar for all samples.

The engineering stress–strain curves determined from the microcompression tests are shown in Fig. 4c. Although the scatter in the curves is significant, we can nevertheless make some general observations. After the initial elastic behavior, the pillars yield at quite different loads with the 35 MPa sample exhibiting the lowest yield stresses. The average yield stress at 2 % plastic strain of the pillar data is summarized in Fig. 4c. The yield stress values of the unworn sample and the sample worn at 15 MPa contact pressure show only little difference. Some pillars tested failed catastrophically before the preset maximum displacement was reached as indicated by the arrows in Fig. 4c. This behavior was more frequently observed in case of the unworn and 15 MPa samples. The 35 MPa sample exhibits less scatter and more pronounced strain hardening than the other two samples. The pillars of the 15 MPa sample appear somewhat stiffer than the other pillars, which exhibit smaller slopes in the elastic portion of the stress–strain curve. Such behavior can, however, be related to misalignment between tip and pillar [19], which we tried to minimize but is difficult to avoid.

Figure 5 shows typical images of the micropillars prior to deformation and after deformation as well as cross sections of the compressed micropillars. The cross section of the unworn pillar (Fig. 5c) shows chunks of silicon close to the surface, marked by white arrows. Similarly, a large silicon particle is seen close to the surface of the pillar on the wear track created with a 15 MPa contact pressure (Fig. 5i). The pillar from the wear track created with a 35 MPa contact pressure (Fig. 5f) shows the lowest amount and smaller pieces of silicon.

Discussion

In this study, we combined different techniques to better understand the third body phenomenon leading to optimal tribological response (i.e., steady-state low friction and wear) of aluminum–steel tribosystems. Sliding experiments were performed using two different contact pressures in order to capture the effects of the input energy on the running-in behavior. Comparing these different sliding conditions in our study, it appears that the higher contact pressure (i.e., 35 MPa) results in low
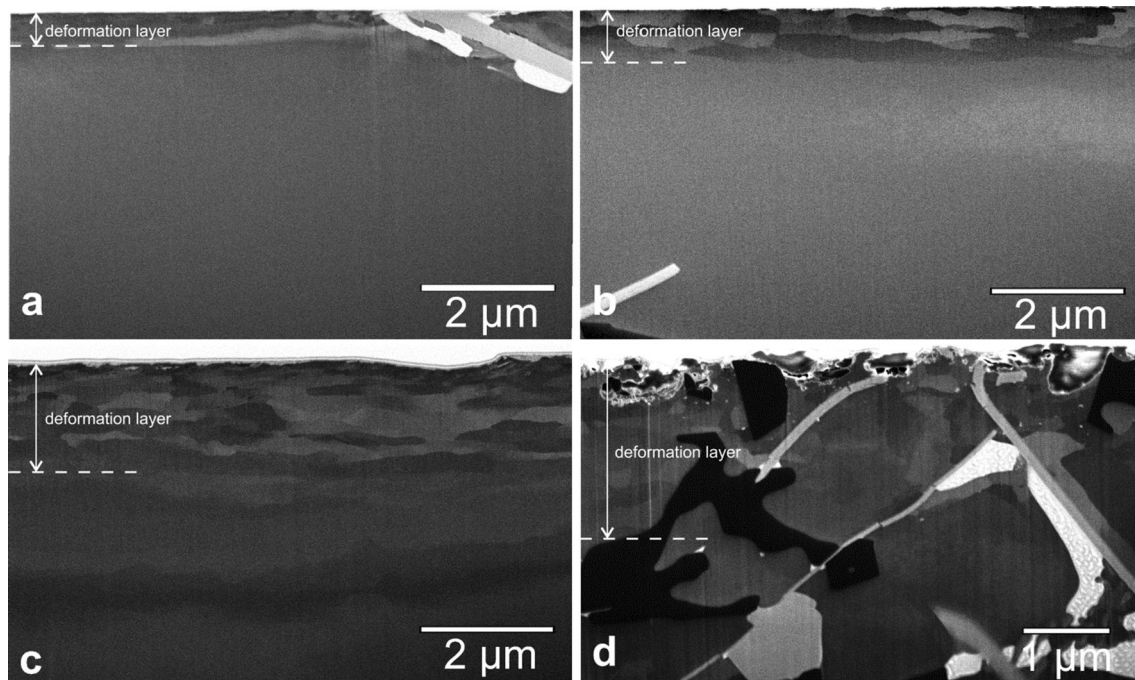
Fig. 3 Cross-sectional SEM images of the near-surface regions of the **a** unworn sample and samples worn at a contact pressure of **b** 35 MPa and **c**, **d** 15 MPa. The grain-refined layer is thinner for 35 MPa and exhibits a well-defined boundary to the bulk material. The changes in grain structure are clearly visible, even in microstructurally less homogeneous parts on the samples. All images were taken at a tilt angle of 52°

friction and wear with a short running-in period, while the lower contact pressure of 15 MPa showed higher friction forces and more wear without reaching steady-state sliding. To elucidate on these variations of the tribological response, we investigated the third bodies in terms of their elemental composition, structure, and mechanical behavior. The worn surfaces for both the low and high contact pressures showed an increase in the oxide content compared to the unworn surface, which is quite common in metallic sliding contacts [20–24], in particular for aluminum alloys [1, 4, 13, 25, 26]. In addition, the cross-sectional SEM images revealed a grain refinement in the near-surface region, which is thicker for the sliding tests performed at a lower contact pressure (i.e., 15 MPa) compared to the higher one (i.e., 35 MPa). The grain refinement in aluminum alloys induced by sliding has been previously reported [1, 4] and can be explained by nucleation of dislocations at the surface as well as rotation of clusters [27, 28].

In general, one would expect a significant deviation in the mechanical response of the worn surfaces compared to the unworn ones [29]. However, in our experiments only small differences of the average values but significant scatter of the data were observed. The large scatter in the hardness of the wear track can be explained by the structure of the MML, which exhibits significant variations in the thickness, as well as by the roughness on the surface. It is unlikely that these fluctuations in the mechanical data are due to the presence of voids, which has been previously reported after sliding on Al-based materials resulting in the formation of a soft layer [9]. The cross-sectional images in our study (Fig. 3) showed no evidence of void formation. At indentation depths larger than approximately 500 nm, the hardness is higher for the wear tracks created with a 15 MPa contact pressure compared to the 35 MPa contact pressure and the unworn surface. This can be explained by the thicker grain-refined layer under these sliding conditions compared to the wear track created with a 35 MPa contact pressure. A less likely reason for the higher hardness values in the 15 MPa test is the increased oxide concentration, which in the form of aluminum oxide would exhibit higher hardness compared to pure Al. However, Al–Ca oxides were found only up to a depth of 500 nm and are thus unlikely to cause the hardness increase at the larger depths. The hardness for indentation depths less than 500 nm, though, may be influenced by the chemical changes, but this effect is very likely masked by the increased hardness of the unworn sample resulting from the sample cutting process and the concomitant deformation layer on the unworn surface. The observed decrease in hardness with increasing depth which has been observed for all samples is similar to hardness changes due to the classical indentation size effect [30]. The indentation size effect was not considered in this study, since our

(a)

(b)

(c)
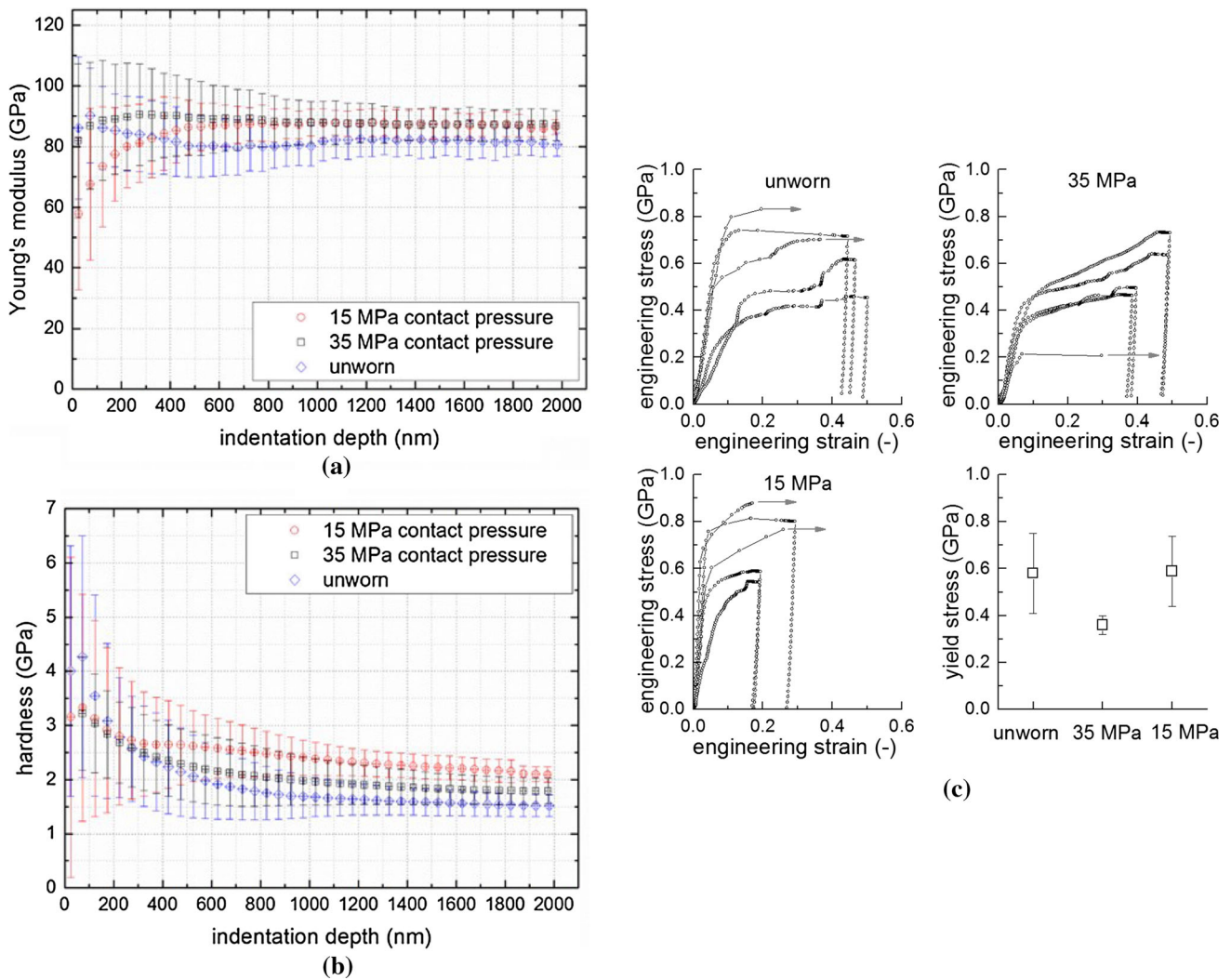
Fig. 4 a Young's modulus and b hardness of the unworn and worn surfaces measured by means of nanoindentation. c Microcompression testing results of the worn and unworn surfaces plotted in terms of the engineering stress versus engineering strain and yield stress at 2 % plastic strain versus the contact pressure used in the sliding experiments

conclusions are based on indentation depths at which an almost constant hardness value has been reached.

The nanoindentation results obtained at the larger indentation depths are confirmed by the microcompression data showing the highest yield stress for the 15 MPa contact pressure sample, which is probably related to the thicker grain-refined layer compared to the 35 MPa sample. The 15 MPa micropillars exhibit little strain hardening and mechanical instabilities, which is apparently related to the presence of the rather large Si particles and counteracted by the fine dispersion of the Si particles in the 35 MPa micropillars. The increased hardness and yield stress of the sub-surface layer of the 15 MPa sliding test indicate a higher shear strength, which correlates well with the higher friction values. The 35 MPa micropillars, on the other hand, exhibit higher mechanical stability in terms of

reduced catastrophic failure and more pronounced strain hardening, which might be a result of dislocation strengthening (i.e., higher dislocation density with a more homogeneous distribution compared to the 15 MPa sliding test). Congruently, the formation of a thin and stable MML, as observed for the 35 MPa contact pressure experiment, is responsible for the short running-in period resulting in low friction and high wear resistance, as also reported in the literature [11, 31].

The difference in the microstructural evolution for the two contact pressures may be explained by the differences in the flow of the tribological circuit [32, 33] comprising the source flow (i.e., material transformation from the first body into the third body), the internal flow (i.e., material movement within the contact), the ejection flow (i.e., ejected material), recirculation flow (i.e., material
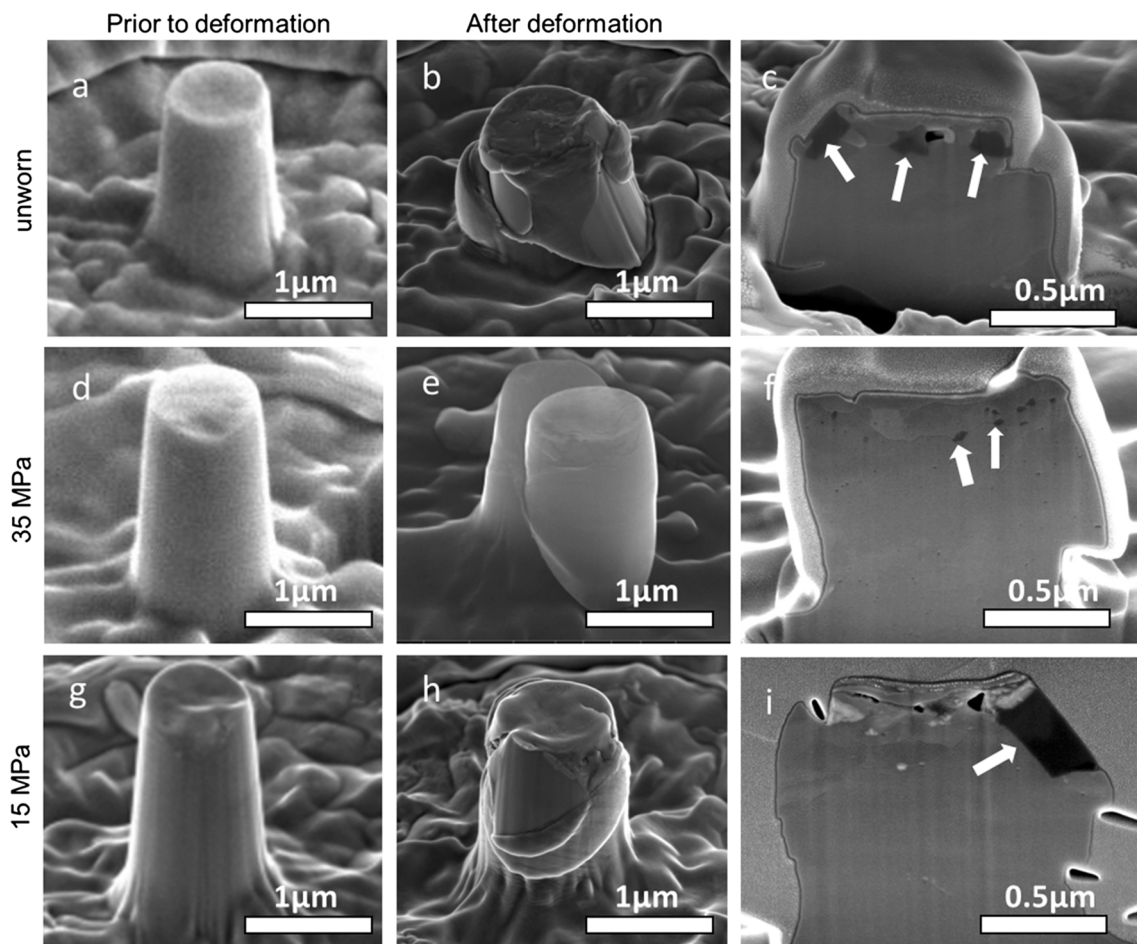
Fig. 5 SEM images of the micropillars before (**a, d, g**) and after (**b, e, h**) the compression tests for the unworn and worn surfaces. **c, f, i** Cross-sectional SEM images of the compressed micropillars. The Si particles are marked by *white arrows*. The micrographs were taken at a tilt angle of 52°

reintroduced to the interface), and the wear flow (i.e., permanently removed material). Considering the flat-on-flat sliding contact in our study, the higher contact pressure leads to a larger and more uniform contact area resulting initially in more contacting asperities. Consequently, the higher degree of asperity collision results in higher frictional forces upon initial sliding (i.e., within the first hour), as observed in Fig. 1a. The high amount of asperity collisions, in combination with possibly the frictional heating, leads to an increase in the source flow and, thus, rapid formation of a thin and uniform MML. The formation of this uniform ∼1-μm-thick layer during the running-in stage averts further deformation within the underlying material resulting in low friction and wear steady-state sliding. The fact that the thickness of the MML can remain nearly constant in the course of an experiment has previously been reported by Rice et al. [14].

In contrast to these sliding conditions, the lower contact pressure experiment showed initially a lower friction force, which can be attributed to the fewer contacting asperities

compared to the higher load test. Subsequently, the third body formation is different under these conditions and does not yield low friction values at any point throughout the experiment. Indeed, initial contact conditions have been previously shown to influence the course of friction in the experiments [16, 34]. Due to the higher friction work dissipated in our system with the lower contact pressure, an overall increase in the oxygen content is observed, possibly as a result of mechanical intermixing [35, 36]. In addition, the higher friction forces lead to the formation of a thicker grain-refined layer in the sub-surface of the lower contact pressure experiments (i.e., 15 MPa). It should be noted that, based on the homogeneous macroscopic wear track of pin and disk, the formation of the harder tribofilm in the case of the 15 MPa contact pressure is not attributed to misaligned or unstable contact between the two surfaces, which could result in inadequate surface adaptation and additional plowing contributions. From the results shown here, it remains unclear whether the higher friction and wear values in the lower contact pressure test are a result of

the thicker grain-refined layer or, conversely, the higher friction work induced the microstructure found at the end of the experiment. This phenomenon is currently being investigated in more detail and will be presented in a future study.

Summary and conclusion

In this study, we evaluated the chemical composition and strength of the near-surface region in aluminum–silicon sliding contacts in order to better understand the running-in behavior resulting in low friction and wear during steady-state. XPS is used to study the atomic concentration with respect to sputtering depth, while cross-sectional SEM analysis is performed to observe the changes in the microstructure. The sliding-induced elemental and structural changes within the sub-surface region correlate with the mechanical properties, which were determined by means of nanoindentation and microcompression. The lower contact pressure experiments resulted in high friction and wear, without reaching steady-state sliding, which was associated with higher degree of mechanical mixing and grain refinement. The nanoindentation and microcompression results correlated well with the chemical and structural changes, indicating higher hardness and yield stress for the experiment with the higher amount of mechanical mixing. Optimal tribosystem response (i.e., short running-in period and low steady-state friction and wear) was achieved by the formation of a thin and mechanically stable tribolayer with a sharp transition to the underlying material.

References

1. Deuis RL, Subramanian C, Yellup JM (1997) Dry sliding wear of aluminium composites—A review. Compos Sci Technol 57:415–435
2. Rohatgi P (1991) Cast aluminum-matrix composites for automotive applications. JOM 43:10–15
3. Godet M (1984) The third-body approach: a mechanical view of wear. Wear 100:437–452
4. Shockley JM, Strauss HW, Chromik RR, Brodusch N, Gauvin R, Irissou E et al (2013) In situ tribometry of cold-sprayed Al-Al$_2$O$_3$ composite coatings. Surf Coat Technol 215:350–356
5. Minami I, Sugibuchi A (2012) Surface chemistry of aluminium alloy slid against steel lubricated by organic friction modifier in hydrocarbon oil. Adv Tribol 2012:7
6. Alshmri F, Atkinson HV, Hainsworth SV, Haidon C, Lawes SDA (2014) Dry sliding wear of aluminium-high silicon hypereutectic alloys. Wear 313:106–116
7. Sarkar AD (1975) Wear of aluminium-silicon alloys. Wear 31:331–343
8. Venkataraman B, Sundararajan G (1996) The sliding wear behaviour of Al-SiC particulate composites—I Macrobehaviour. Acta Mater 44:451–460
9. Venkataraman B, Sundararajan G (1996) The sliding wear behaviour of Al-SiC particulate composites—II. The characterization of subsurface deformation and correlation with wear behaviour. Acta Mater 44:461–473
10. Rosenberger MR, Schvezov CE, Forlerer E (2005) Wear of different aluminum matrix composites under conditions that generate a mechanically mixed layer. Wear 259:590–601
11. Venkataraman B, Sundararajan G (2000) Correlation between the characteristics of the mechanically mixed layer and wear behaviour of aluminium, Al-7075 alloy and Al-MMCs. Wear 245:22–38
12. Rosenberger MR, Forlerer E, Schvezov CE (2009) Wear behavior of AA1060 reinforced with alumina under different loads. Wear 266:356–359
13. Li XY, Tandon KN (1999) Mechanical mixing induced by sliding wear of an Al-Si alloy against M2 steel. Wear 225:640–648
14. Rice SL, Nowotny H, Wayne SF (1981) Characteristics of metallic subsurface zones in sliding and impact wear. Wear 74:131–142
15. Sauger E, Fouvry S, Ponsonnet L, Kapsa P, Martin JM, Vincent L (2000) Tribologically transformed structure in fretting. Wear 245:39–52
16. Blau PJ (2008) Friction science and technology: from concepts to applications, 2nd edn. Taylor & Francis, Boca Raton
17. Feser T, Stoyanov P, Mohr F, Dienwiebel M (2013) The running-in mechanisms of binary brass studied by in-situ topography measurements. Wear 303:465–472
18. Jacobson B (2003) The Stribeck memorial lecture. Tribol Intern 36:781–789
19. Schwaiger R, Weber M, Moser B, Gumbsch P, Kraft O (2012) Mechanical assessment of ultrafine-grained nickel by microcompression experiment and finite element simulation. J Mater Res 27:266–277
20. Stoyanov P, Romero PA, Järvi TT, Pastewka L, Scherge M, Stemmer P et al (2013) Experimental and numerical atomistic investigation of the third body formation process in dry tungsten/tungsten-carbide tribo couples. Tribol Lett 50:67–80
21. Rigney DA, Fu XY, Hammerberg JE, Holian BL, Falk ML (2003) Examples of structural evolution during sliding and shear of ductile materials. Scr Mater 49:977–983
22. Rigney DA (1997) Comments on the sliding wear of metals. Tribol Intern 30:361–367
23. Stoyanov P, Merz R, Romero PA, Wählisch FC, Abad OT, Gralla R et al (2015) Surface softening in metal-ceramic sliding contacts: an experimental and numerical investigation. ACS Nano 9:1478–1491
24. Stoyanov P, Stemmer P, Järvi T, Merz R, Romero P, Scherge M et al (2013) Friction and wear mechanisms of tungsten-carbon systems: a comparison of dry and lubricated conditions. ACS Appl Mater Interfaces 5(6123):6135
25. Li XY, Tandon KN (2000) Microstructural characterization of mechanically mixed layer and wear debris in sliding wear of an Al alloy and an Al based composite. Wear 245:148–161
26. Kim HJ, Windl W, Rigney D (2007) Structure and chemical analysis of aluminum wear debris: experiments and ab initio simulations. Acta Mater 55:6489–6498
27. Fischer A (2009) Subsurface microstructural alterations during sliding wear of biomedical metals. Modelling and experimental results. Comput Mater Sci 46:586–590
28. Rigney DA (2000) Transfer, mixing and associated chemical and mechanical processes during the sliding of ductile materials. Wear 245:1–9

29. Farhat ZN, Ding Y, Northwood DO, Alpas AT (1996) Effect of grain size on friction and wear of nanocrystalline aluminum. Mater Sci Eng A 206:302–313

30. Nix WD, Gao H (1998) Indentation size effects in crystalline materials: a law for strain gradient plasticity. J Mech Phys Solids 46:411–425

31. Shockley JM, Descartes S, Irissou E, Legoux JG, Chromik RR (2014) Third body behavior during dry sliding of cold-sprayed Al-Al$_2$O$_3$ composites. In Situ tribometry and microanalysis. Tribol Lett 54:191–206

32. Descartes S, Berthier Y (2002) Rheology and flows of solid third bodies: background and application to an MoS1.6 coating. Wear 252:546–556

33. Berthier Y (2005) Third-body reality -consequences and use of the third-body concept to solve friction and wear problems. In: Stachowiak GW (ed) Wear—materials, mechanisms and practice. John Wiley and Sons, Ltd., Chichester, pp 291–316

34. Scherge M, Shakhvorostov D, Pöhlmann K (2003) Fundamental wear mechanism of metals. Wear 255:395–400

35. Young JL, Kuhlmann-Wilsdorf D, Hull R (2000) The generation of mechanically mixed layers (MMLs) during sliding contact and the effects of lubricant thereon. Wear 246:74–90

36. Furlong O, Miller B, Tysoe W (2011) Shear-induced surface-to-bulk transport at room temperature in a sliding metal-metal interface. Tribol Lett 41:257–261